



|              |   |
|--------------|---|
| Title        | Acid Responsive Hydrogen-Bonded Organic Frameworks                                  |
| Author(s)    | Hisaki, Ichiro; Suzuki, Yuto; Gomez, Eduardo et al.                                 |
| Citation     | Journal of the American Chemical Society. 2019, 141(5), p. 2111-2121                |
| Version Type | AM  |
| URL          | <a href="https://hdl.handle.net/11094/92728">https://hdl.handle.net/11094/92728</a> |
| rights       | © 2019 American Chemical Society  |
| Note         |   |

*The University of Osaka Institutional Knowledge Archive : OUKA*

<https://ir.library.osaka-u.ac.jp/>

The University of Osaka

# Acid Responsive Hydrogen-Bonded Organic Frameworks

Ichiro Hisaki,<sup>†\*</sup> Yuto Suzuki,<sup>‡</sup> Eduardo Gomez,<sup>‡#</sup> Qin Ji,<sup>†</sup> Norimitsu Tohnai,<sup>‡</sup> Takayoshi Nakamura,<sup>†</sup> Abderrazzak Douhal<sup>#\*</sup>

<sup>†</sup>Research Institute for Electronic Science, Hokkaido University, Kitaku, Sapporo, Hokkaido 001-0020, Japan

<sup>‡</sup>Department of Material and Life Science, Graduate School of Engineering, Osaka University, 2-1 Yamadaoka, Suita, Osaka 565-0871, Japan.

<sup>#</sup> Departamento de Química Física, Facultad de Ciencias Ambientales y Bioquímica, and INAMOL, Universidad de Castilla-La Mancha, Avenida Carlos III, S/N, 45071 Toledo, Spain.

**ABSTRACT:** A porous hydrogen-bonded organic framework (HOF) responsive to acid was constructed from hexaazatrinaphthylene derivatives with carboxy phenyl groups (CPHATN). Precise structures of both 1,2,4-trichlorobenzene solvate [CPHATN-1(TCB)] and activated HOF with permanent porosity (CPHATN-1a) were successfully determined by single-crystalline X-ray diffraction analysis. Permanent porosity of CPHATN-1a was evaluated by gas sorption experiments at low temperature. CPHATN-1a also shows significant thermal stability up to 633 K. Its crystals exhibit a rich photochemistry thanks to intramolecular charge-transfer and interunits proton-transfer reactions. Femtosecond (fs) experiments on crystals demonstrate that these events occur in  $\leq 200$  fs and 1.2 ps, respectively. Moreover, single crystal fluorescence microscopy reveals a shift of the emission spectra most probably as a result of defects, and a high anisotropic behavior, reflecting an ordered crystalline structure with a preferential orientation of the molecular dipole moments. Remarkably, CPHATN-1a, as a result of the protonation of pyridyl nitrogen atoms embedded in its  $\pi$ -conjugated core, shows a reversible vapor acid-induced color changes from yellow to reddish-brown, which can be also followed by an ON/OFF of its emission. To the best of our knowledge, this is the first HOF that exhibits acid-responsive color changes. The present work provides new findings for developing stimuli responsive HOFs.

## INTRODUCTION

Porous organic framework with well-defined organic components and pores is one of the most attractive functional materials applicable not only for storage and separation of gases and organic molecules, but for organic electronic devices and sensors.<sup>1</sup> Since O. Yaghi and his co-workers reported pioneering works on covalent organic frameworks (COFs),<sup>2</sup> the field of porous organic materials has come to the forefront of science and technologies.<sup>3</sup> The materials built from molecules through hydrogen bonding, known as hydrogen-bonded organic frameworks (HOFs)<sup>4</sup> or supramolecular organic frameworks (SOFs)<sup>5</sup> also attracts much attention recently because, in contrast to COFs, HOFs are able to be isolated high-crystalline materials, such as single crystals in many cases, due to their reversible hydrogen bond formation and deformation. This allows to reveal their structures precisely based on single crystal X-ray diffraction (SXRD) analysis, and therefore, to investigate structure-property relationship. HOFs can be also regenerable<sup>6</sup> and flexible<sup>7</sup> due to the above mentioned bond feature. Fragility, on the other hand, have prevented HOFs to be applied as a functional porous materials. The structures often collapse during removal of solvent molecules from pores of the solvated frameworks. Furthermore, even when molecular structures and hydrogen-bonding manners were pre-designed well, the molecules do not always yield the desired porous

HOFs, but result into unexpected nonporous materials. Establishment of universal design strategy and creation of new functionality, such as external-stimuli responsiveness, are still developing, although a number of HOFs have been reported.<sup>8</sup>

In connection with this, we previously proposed that  $C_3$  symmetric  $\pi$ -conjugated molecules with three *o*-bis(carboxyphenyl)aryl groups in periphery were able to be applied for constructing HOFs<sup>9</sup> and achieved significantly stable HOFs with permanent porosity.<sup>10</sup> To develop external stimuli responsive fluorescent HOFs with permanent porosity, we next designed carboxyphenyl-substituted hexaazatrinaphthylene<sup>11</sup> derivatives (CPHATN) as a building block.

Introducing nitrogen atoms into polycyclic aromatic hydrocarbons are capable of (1) fine-tuning of frontier orbital levels, lowering LUMO levels in many cases, (2) coordinating with metal cations, and (3) interacting with cationic species such as metal ions, proton, and other organic cations. After establishment of a facile synthetic route,<sup>12</sup> HATN and its analogues have been widely applied for electron transporting materials,<sup>13</sup> ligands of novel metal complexes,<sup>14</sup> receptor for cations,<sup>15</sup> catalyst,<sup>16</sup> single-molecular magnet,<sup>17</sup> cathode of lithium battery,<sup>18</sup> and metal-organic framework,<sup>19</sup> in addition for a mesogen of liquid crystals.<sup>20</sup> More recently, HATN segments are used for constructing COFs applicable hydrogen storage,<sup>21</sup> lithi

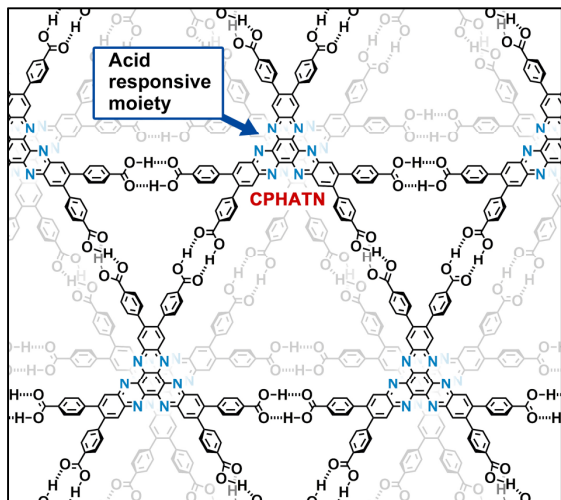


**Figure 1.** A porous layered assembly of H-HexNets based on HATN derivative (CPHATN), which has acid responsive moieties.

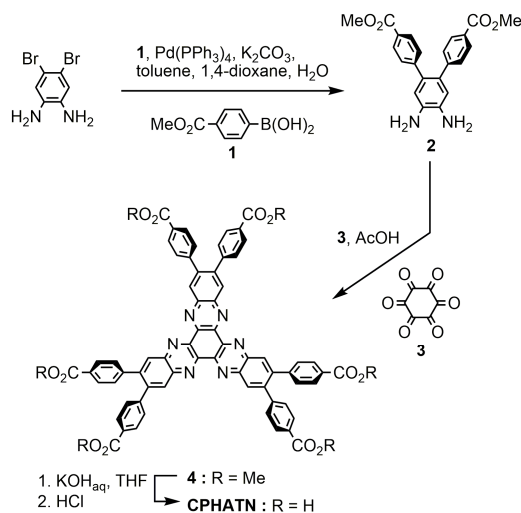
um battery,<sup>22</sup> Pb(II) cation scavenger,<sup>23</sup> and catalyst.<sup>24</sup> However, no examples of HOFs based on HATN has been reported so far.

In this work, we report an acid-responsive, extremely thermostable HOF with permanent porosity by using carboxyphenyl-substituted hexaazatrinaphthylene derivative CPHATN. We revealed that CPHATN formed hydrogen-bonded hexagonal network (H-HexNet),<sup>8</sup> which is stacked without interpenetration to give a layered HOF (Figure 1). The HOF can be prepared by facile recrystallization. The activated HOF (CPHATN-1a) retains its porous structures up to at least 633 K and is basically stable against common organic solvents. Femtosecond emission spectroscopy unravels that the photobehaviour of the excited crystals is shaped by ultrafast intramolecular charge-transfer and proton-transfer events happening in  $\leq 200$  fs and 1.2 ps, respectively. Space- and time-resolved fluorescence microscopy shows that cracks and expected defects in the crystals affect the emission spectra and lifetime. We also observed that single crystals exhibit a high anisotropic behavior reflecting a strongly ordered system. Very interestingly, CPHATN-1a changes its color reversibly from yellow to reddish-brown when exposed to acids, and its fluorescence can be switched OFF or ON in presence or removing of acid vapors. This is, to the best of our knowledge, the first example of HOFs with external-stimuli responsiveness in color and emission. The present results would open a door to develop a new porous materials with stimuli responsiveness.

## RESULTS AND DISCUSSION

**Synthesis and crystallization of CPHATN.** 4,5-bis(methoxycarboxyphenyl)-1,2-diaminobenzene (**2**) was synthesized by Suzuki-Miyaura cross-coupling reaction of 4,5-dibromo-1,2-diaminobenzene and 4-methoxycarbonylphenylboronic acid (**1**). Diaminobenzene derivative **2** was treated with cyclohexanehexone (**3**) in acetic acid to give ester derivative **4**, which was subsequently hydrolyzed to give CPHATN. Crystallization was preliminarily attempted by using a mixed solution of dimethylacetamide (DMAA) and methyl benzoate (MeBz) at 333 K, resulting non-porous crystal CPHATN-NP (Figure S1), in which carboxy groups of CPHATN were trapped by solvent molecules via hydrogen bonds, preventing formation of a H-HexNet. Finally, slow evaporation of a mixed solution of *N*-methylpyrrolidone (NMP) and 1,2,4-trichlorobenzene (TCB) at 373 K for 12 h allowed to yield a block-shaped *P*-1 crystal [CPHATN-1(TCB)], which has a layered structure of H-HexNet frameworks.

### Scheme 1. Synthesis procedure of hexaazatrinaphthylene derivatives CPHATN.



**Thermal Behaviors of CPHATN-1(TCB).** Thermogravimetric (TG) analysis of CPHATN-1(TCB) shows that solvent molecules accommodated in the channel were completely removed at 527 K and the resultant desolvated state was kept up to ca. 673 K (Figure 2a). The weight loss of 22% indicates that CPHATN-1(TCB) contains TCB with a host-guest ratio of 1:2 (calc. 24.7%). Next, to reveal structural changes of CPHATN-1(TCB) during desolvation by heating, we recorded temperature variable powder X-ray diffraction (VT-PXRD) patterns of as-formed crystalline bulks of CPHATN-1(TCB) from room temperature to 633 K, which is the upper limit temperature of the apparatus we used (Figure 2b). Although the initial patterns are not clear due to bulk solvent attached on the crystalline surface and sever

disorder of solvent molecules accommodated in voids, peaks gradually appeared by heating. Weak but unambiguous peaks at 4.30, 5.18, 8.62, and 10.48° started to appear at 356 K, and these peaks are slightly shifted into wider angle up to 387 K, indicating subtle shrinkage of the crystallographic cell. The peak intensity increased as heating, reached plateau at ca. 523 K, and remained up to 633 K (Figure 1b,c). These results indicate that the desolvated framework is stable and rigid sufficiently to retain the structure under high temperature.

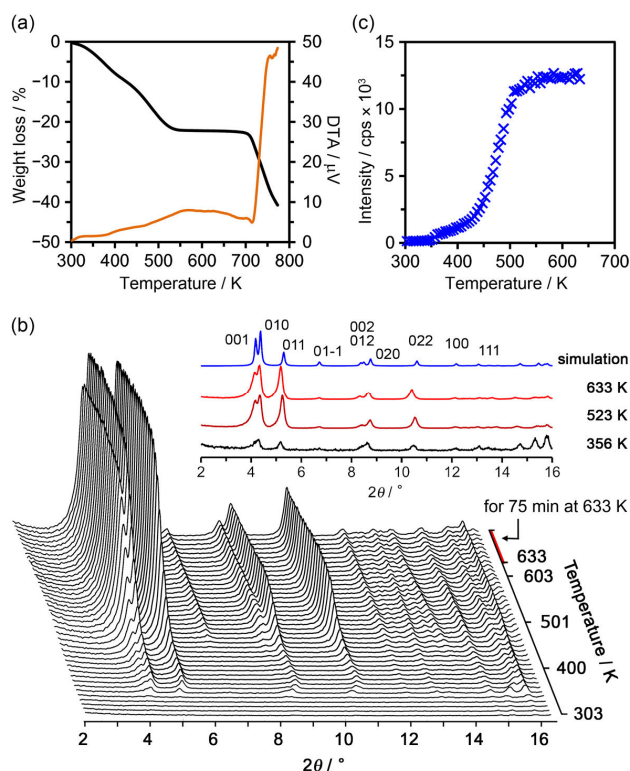


**Figure 2.** Thermal behavior of crystalline bulk of as-formed **CPHATN-1(TCB)**. (a) TG-DTA profile of **CPHATN-1(TCB)**. (b) VT-PXRD measurements of **CPHATN-1(TCB)** heated from room temperature to 633 K. Inset: typical PXRD patterns during heating. (c) Changes of the 010 peak intensity with temperature. For VT-PXRD measurement, temperature was raised at the rate of 1 K/min. PXRD patterns were recorded from 2° to 17° of  $2\theta$  with the scan rate of 3°/min. Therefore, each scan has a temperature gradient of 5 K.  $\lambda = 1.54056 \text{ \AA}$

Judging from the thermal behavior of the frameworks mentioned above, activation of **CPHATN-1(TCB)** was accomplished by heating at 463 K for 72 h under a vacuum condition, giving the corresponding desolvated materials **CPHATN-1a** possessing permanent porosity. Complete desolvation and crystallinity of the activated materials were confirmed by  $^1\text{H}$  NMR spectra of solutions

dissolved in deuterated DMSO (Figure S2) and PXRD patterns (Figure S3), respectively.

**Crystal Structures of CPHATN-1(TCB) and CPHATN-1a.** In *P*-1 crystal **CPHATN-1(TCB)**, *o*-bis(carboxyphenyl)benzene moieties form a triangular hydrogen bonded motif so-called phenylene triangle (PhT) motif<sup>8</sup> to give a H-HexNet sheet, which then stacks without interpenetration to give a layered assembly of H-HexNet (Figure 3a). The **CPHATN** core is slightly deformed due to packing force: root mean square deviation (RMSD) of the **CPHATN** core is 0.142 Å. An H-HexNet layer tightly stacks with the adjacent layers in two ways (Figure 3b). A **CPHATN** core in the first layer (yellow) stacks tightly with a core in the second layer (cyan) with N...N distance of 3.08 Å. Interplanar distances between mean planes of the stacked **CPHATN** cores is 2.90 Å. The other stacking way is that the cores in the second (cyan) and third (dark blue) layers are overlapped between edges of the cores: the interplanar distances is 3.13 Å. The framework has a one-dimensional channel along the crystallographic *a* axis, and TCB molecules used for crystallization are accommodated in the channel, although they severely disordered, and therefore, are not able to be solved crystallographically. A ratio of total potential solvent area volume calculated by PLATON software was 26% (cell volume: 3190.3 Å<sup>3</sup>, void volume per cell: 843.0 Å<sup>3</sup>).

It is noteworthy that the materials after activation partly retained single crystallinity, allowing to accomplish SXRD analysis of **CPHATN-1a**. As shown in Table 1, mainly length of the *b* axis was shortened by 1.4 Å and the  $\gamma$  got smaller by 4.3°. The refined structure is shown in Figure 3e-g. These changes in the cell parameters were brought particularly from deformation in one of the carboxy dimers having conformational frustration<sup>9a,b</sup> (for more detail, see Figure S4), while relative positions of the stacked **CPHATN** cores remained (Figure 3c,f). The interplanar distances between cores in the 1<sup>st</sup>-2<sup>nd</sup> layers and the 2<sup>nd</sup>-3<sup>rd</sup> layers are 2.89 and 3.09 Å, respectively, and the shortest N...N distance is 3.08 Å. As shown in Figure 3g, one-dimensional pores with a triangular cross section with width of 8.8 Å are formed along the *c* axis. The wall of the channel has branched small spaces with diameter of ca. 3 Å. A ratio of total potential solvent area volume was 20% (cell volume: 2989.6 Å<sup>3</sup>, void volume per cell: 608.1 Å<sup>3</sup>).

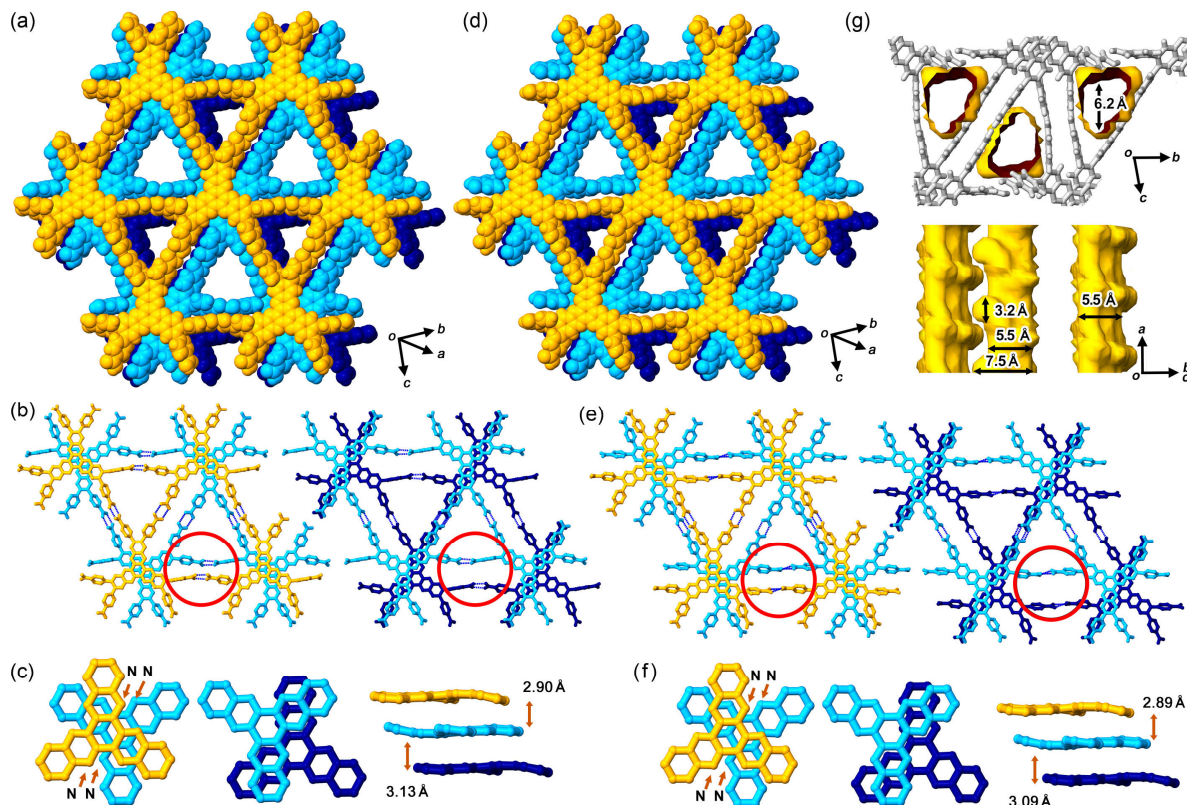


**Figure 3.** Crystal structures of solvate **CPHATN-1(TCB)** (a,b,c) and activated form **CPHATN-1a** (d,e,f). (a,d) Three layers of the stacked HexNet sheets, where 1<sup>st</sup>, 2<sup>nd</sup>, and 3<sup>rd</sup> layers are colored yellow, cyan, and blue, respectively. (b,e) Relative orientation of the stacked 1<sup>st</sup>-2<sup>nd</sup> and 2<sup>nd</sup>-3<sup>rd</sup> layers (left and right, respectively). (c,f) Relative orientation of the stacked cores: 1<sup>st</sup>-2<sup>nd</sup> cores (left), 2<sup>nd</sup>-3<sup>rd</sup> cores (middle), and side view of the stacking (right). (g) Visualized surface of the activated void in **CPHATN-1a** with the Mercury software. In crystal structure of **CPHATN-1(TCB)**, solvent molecules (TCB) are accommodated in the voids, but is severely disordered. Red circles in (a,e) refer the conformationally frustrated carboxy dimers, which experience structural changes upon activation.

**Table 1.** Crystal data of **CPHATN-1(TCB)** and **CPHATN-1a**

|                            | <b>CPHATN-1(TCB)</b> | <b>CPHATN-1a</b> | difference |
|----------------------------|----------------------|------------------|------------|
| Space group                | <i>P</i> -1          | <i>P</i> -1      |            |
| <i>a</i> [Å]               | 7.27754(17)          | 7.3893(4)        | +0.111     |
| <i>b</i> [Å]               | 20.8039(4)           | 19.3980(11)      | -1.406     |
| <i>c</i> [Å]               | 21.7135(4)           | 21.3787(10)      | -0.335     |
| $\alpha$ [°]               | 76.5118(17)          | 80.108(4)        | +3.60      |
| $\beta$ [°]                | 89.6714(17)          | 88.822(4)        | -0.85      |
| $\gamma$ [°]               | 86.3993(18)          | 82.022(5)        | -4.38      |
| <i>V</i> [Å <sup>3</sup> ] | 3190.33(12)          | 2989.6(3)        | -200.73    |

**Structure Durability toward Common Solvents.** To disclose structural durability of the framework toward

common solvents, crystalline powder of **CPHATN-1a** was soaked into hot solvents [chloroform (333 K), toluene (373 K), ethanol (333 K), and water (373 K)] for 24 h. After filtered, the samples were subjected to PXRD measurement. The original pattern of **CPHATN-1a**, was retained for these solvents after filtration and the peak intensity was recovered after heating the sample to remove the solvent (Figure 4). Furthermore, it is remarkable that **CPHATN-1a** was regenerated even after soaked in strong acid: although the PXRD pattern of the HCl-soaked sample was once decayed significantly, the original pattern was recovered after removing HCl by heating.

**Evaluation of Permanent Porosity.** The permanent porosity of **CPHATN-1a** was evaluated by nitrogen, oxygen, carbon dioxide, and hydrogen sorption measurements at 77 K, 77 K, 195 K, and 77 K, respectively (Figure S5). **CPHATN-1a** shows type-I sorption isotherms for all gasses, indicating that it has micro pore. The uptakes are 108.7 cm<sup>3</sup>/g for N<sub>2</sub> at 99.7 kPa, 144 cm<sup>3</sup>/g for

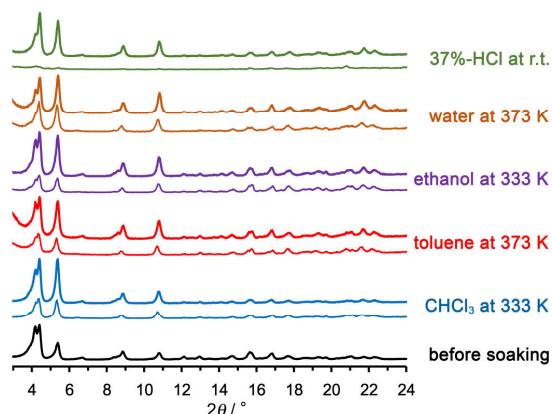


**Figure 4.** PXRD patterns of crystalline bulk of **CPHATN-1a** before and after soaking into hot solvents for 24 h. Thin lines: after filtration. Bold lines: after heating the filtered samples at 423 K for 1h to remove the solvents.

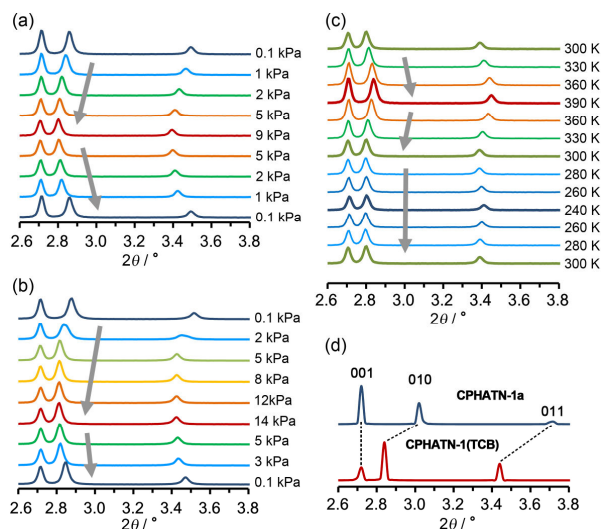


**Figure 5.** PXRD pattern changes of **CPHATN-1a** upon sorption of (a) benzene and (b) hexane vapor. (c) VT-PXRD patterns of benzene-filled material **CPHATN-1(Ben)**. (d) Simulated patterns of **CPHATN-1(TCB)** and **CPHATN-1a**. The diffraction patterns were recorded with synchrotron X-ray radiation with wavelength of 1.000 Å.

O<sub>2</sub> at 20.9 kPa, 116.0 cm<sup>3</sup>/g for CO<sub>2</sub> at 100.4 kPa, and 71.9 mL for H<sub>2</sub> at 101.7 kPa. The calculated BET surface area and pore size based on a N<sub>2</sub> sorption isotherm are 379 m<sup>2</sup>g<sup>-1</sup> and 0.78 nm, respectively.

To investigate precise structural changes upon sorption of hydrocarbons, PXRD patterns of **CPHATN-1a** were recorded upon introducing vapors of benzene and hexane (Figure 5a,b). The 010 and 011 diffraction peaks are shifted into the small angle region upon vapor

absorption, while the 001 peak remained the original position during the sorption. Furthermore, when the benzene-filled material **CPHATN-1(Ben)** was heated, the 010 and 011 peaks were shifted into the wide angle region, indicating shrink of the cell due to release of benzene molecules (Figure 5c). These structural changes consist to crystal structures of **CPHATN-1(TCB)** and **CPHATN-1a** (Figure 5d).

#### Steady-State Absorption and Emission Studies.

Figure 6a shows the absorption and emission spectra of **CPHATN-1a** in solid state, which display intensity maxima at 447 and 539 nm, respectively. The shoulder at around 500 nm reflects the So→S<sub>1</sub> transition onset. The absorption band displays a large full-width at half-maximum (FWHM) (~27000 cm<sup>-1</sup>), which probably reflects the existence of different absorbing species or strong spectral overlap of So→S<sub>1</sub> and So→S<sub>2</sub> bands. Recently, we have reported on the photobehaviour of **CPHAT** and **CBPHAT** materials, which have similar fundamental units.<sup>10</sup> The difference between these materials and the one here studied is the presence of an extra benzene ring joined to each pyrazine group (Figure 1). Comparing their UV-visible absorption spectra, we observe a large bathochromic shift of **CPHATN-1a** one (447 nm) with respect to those of **CPHAT** (392 nm) and **CBPHAT** (404 nm). This reflects a larger π-conjugation in the molecular frame of **CPHATN-1a** produced due to the core by the addition of the three extra benzene groups, as it has been observed in other studied molecules.<sup>25</sup>

The emission spectrum of **CPHATN-1a** has an intensity maximum at 539 nm and displays a large red-shifted band in comparison with those of **CPHAT** (470 nm) and **CBPHAT** (491 nm) ones. The shift is explained by an increment in the π-conjugation in the core of the fundamental units of the material. Moreover, the FWHM of **CPHATN-1a** emission band is ~1900 cm<sup>-1</sup>, smaller than those of **CPHAT-1a** (3300 cm<sup>-1</sup>) and **CBPHAT-1a** (2900 cm<sup>-1</sup>).

The fluorescence excitation spectra of **CPHATN-1a** do not depend on the observation wavelength, but display different spectral shapes when compared to that of the absorption one (Figures 6a and S8). Furthermore, they exhibit intensity maxima at 370 and 504 nm. The different shape of the excitation spectra suggests the opening of efficient non-radiative channels when exciting at wavelengths between 400 and 500 nm. Based on the structure of the fundamental units, we consider that the unpaired electrons of the six nitrogen atoms, which form the core, make more efficient the non-radiative channels due to the coupling with (n,π\*) states.<sup>10</sup> The shape and peaks positions in the excitation spectra also suggest that the absorption at 370 and 504 nm are originated by the So→S<sub>2</sub> and So→S<sub>1</sub> transitions, respectively.

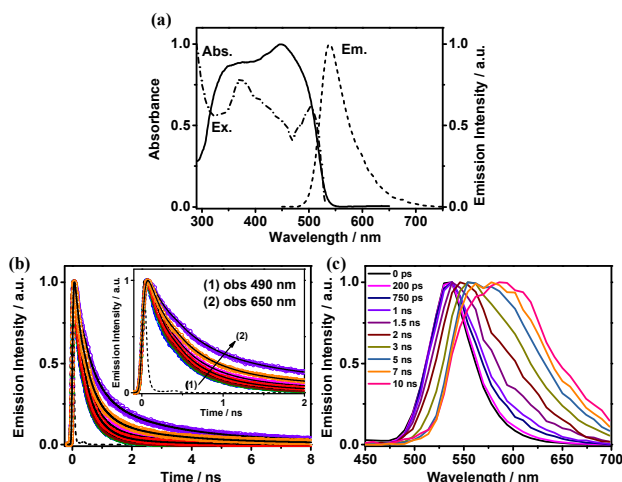


**Figure 6.** a) (solid line) UV-visible absorption, (dashed line) emission, and (dash dot) excitation spectra of the crystals ensemble of **CPHATN-1a**. The excitation wavelength was 370 nm. b) Magic-angle emission decays of the solid of **CPHATN-1a**, upon excitation at 371 nm, and recording at the indicated wavelengths. The solid lines are from the best global fit using a multiexponential function. c) Normalized time-resolved emission-spectra (TRES) of the ensemble solid of **CPHATN-1a**. The excitation wavelength was 371 nm and gating at the indicated delay times.

**Picosecond Time-Resolved Experiments.** To elucidate the behavior of the excited species in the crystals, we carried out picosecond time-resolved emission experiments<sup>26</sup> on **CPHATN-1a** (Figure 6b). The decays exhibit a multiexponential behavior with time constants of 190 and 507 ps and 2.51 ns. All the components are decaying along the whole observation range. The contribution of the fastest component (190 ps) in the emission decay decreases at longer wavelengths, while that of the slowest one (2.51 ns) appears from 550 nm (the intensity maximum of the steady-state spectrum) (Table 2). We suggest that the shortest component corresponds to the emission from the initially excited species, while that of the slowest decay reflects emitting structures formed after an ultrafast event in the formers. We believe that this photoinduced process is an intermolecular proton-transfer between two acid groups of the fundamental units in the crystals (Figure 1). It is worth mentioning that the time-resolution of the setup ( $\sim 30$  ps) does not allow to get the accurate time constant of the process. We will discuss the ultrafast events in the femtosecond part. However, to support the above assignment, we have to take into account the H-bond interactions between the acid groups, and the  $\pi$ - $\pi$  stacking between the core units. For **T12-apo** (HOF), we have previously reported the presence of two different kind of crystals, whose photobehaviour is conditioned by the main acting force in the crystal formation and stabil-

ity.<sup>25d</sup> We found that the value of the fluorescence lifetime of excited **T12-apo** crystals is 20 ns when the main force between the core units forming the crystals interactions is due to  $\pi$ - $\pi$  stacking, and 8.5 ns for the H-bond ones. While **T12-apo** core does not contain nitrogen atoms, allowing  $\pi$ - $\pi$  stacking between their units, **CPHATN-1a**, which has six nitrogen in its core, will have difficulties to pack up by  $\pi$ - $\pi$  interactions, due to the repulsion forces between the no-bonding orbitals of the nitrogen atoms. Therefore, the main signal of emission will be from crystals formed by the H-bonds interactions, contrary to those of  $\pi$ - $\pi$  stacking.

We assign the intermediate component (507 ps) to the emission of species produced after an intramolecular charge transfer (ICT) from the phenyl groups to the main core. **T12-apo** HOF undergoes an ICT event and the time of the emitting species is  $\sim 5$  ns.<sup>10a,25c</sup> The lifetimes of **CPHATN-1a** (190 and 507 ps and 2.51 ns) are much shorter than those of **T12-apo** ( $\sim 1$ ,  $\sim 5$ ,  $\sim 8$  ns). This difference is due to the presence of unpaired electrons on the nitrogen atoms in the **CPHATN-1a** core, opening a non-radiative coupling with not fluorescent ( $n$ ,  $\pi^*$ ) states, making faster the emission decays. It also explains the shape of the excitation spectra at shorter absorption wavelengths.

To get more information on the excited state photo-behaviour, we recorded ps time-resolved emission spectra (TRES). Figures 6c and S9 show the normalized and not normalized TRES of the ensemble solid of **CPHATN-1a**. To begin with, gating at times shorter than 300 ps, the spectra have their intensity maxima at  $\sim 538$  nm with a FWHM of  $1800$   $\text{cm}^{-1}$ , which is very close in value to the one of the steady state spectrum ( $1900$   $\text{cm}^{-1}$ ), suggesting that the species at longer times exhibits a very lower fluorescence quantum yield. The TRES gated at longer times ( $\geq 400$  ps) clearly show a red shift in their intensity maxima, and at 10-ns gating time, the intensity maximum is at 590 nm. In addition to that, the spectra become wider (FWHM= $3200$   $\text{cm}^{-1}$ ), reflecting the emission from different species. Moreover, the Stock shift between the intensity maximum of the excitation spectrum (504 nm from the  $S_0 \rightarrow S_1$  transition) and the maximum of the TRES at longer gating times is large ( $2900$   $\text{cm}^{-1}$ ), suggesting that an intermolecular proton-transfer is occurring at the excited state, as we comment before.

The excitation spectrum displays two bands (Figure 6a), we excited at other wavelengths (433 and 470 nm) to explore the nature of these bands. Figure S10 exhibits the emission decays up both excitations, while Table S3 gives the obtained values from the best fits. The difference in the lifetimes values, using the three excitation wavelengths, is within the expected error from the experiments and fits, indicating that the emitting species are very similar. However, comparing the contribution of the shortest component at the bluest part of the emission band, we observe an increase from 55% (exciting at 371

**Table 2: Values of time constants ( $\tau_i$ ), normalized (to 100) pre-exponential factors ( $a_i$ ) and the contributions ( $c_i = \tau_i \times a_i$ ) obtained from a global multiexponential fit of the emission decays of the ensemble solid of CPHATN-1a, upon excitation at 371 nm and observation as indicated.**

| Sample                                | $\lambda_{\text{obs}}$<br>(nm) | $\tau_1$ (ps)<br>$\pm 30$ ps | $A_1$ | $c_1$ | $\tau_2$ (ps)<br>$\pm 50$ ps | $A_2$ | $c_2$ | $\tau_3$ (ns)<br>$\pm 0.2$ ns | $A_3$ | $c_3$ |
|---------------------------------------|--------------------------------|------------------------------|-------|-------|------------------------------|-------|-------|-------------------------------|-------|-------|
| Ensemble solid of<br><b>CPHATN-1a</b> | 490                            |                              | 59    | 35    |                              | 41    | 65    |                               | -     | -     |
|                                       | 510                            |                              | 55    | 33    |                              | 45    | 67    |                               | -     | -     |
|                                       | 530                            |                              | 54    | 32    |                              | 46    | 68    |                               | -     | -     |
|                                       | 540                            |                              | 54    | 32    |                              | 45    | 61    |                               | 1     | 7     |
|                                       | 550                            | 190                          | 53    | 28    | 507                          | 45    | 62    | 2.51                          | 2     | 10    |
|                                       | 570                            |                              | 48    | 23    |                              | 48    | 57    |                               | 4     | 20    |
|                                       | 590                            |                              | 42    | 15    |                              | 51    | 50    |                               | 7     | 35    |
|                                       | 610                            |                              | 32    | 9     |                              | 54    | 40    |                               | 14    | 51    |
|                                       | 650                            |                              | 20    | 4     |                              | 54    | 28    |                               | 26    | 68    |

**Table 3: Values of time constants ( $\tau_i$ ) and normalized (to 100) pre-exponential factors ( $a_i$ ) obtained from the best fit of the femtosecond emission decays of the ensemble solid of CPHATN-1a, upon excitation at 400 nm and observation as indicated. The negative sign of  $a_i$  indicates a rising component in the emission signal**

| Sample                                | $\lambda_{\text{obs}}$ (nm) | $\tau_1$ (ps) | $A_1$ | $\tau_2$ (ps) | $A_2$ | $\tau_3$ (ps)* | $A_3$ |
|---------------------------------------|-----------------------------|---------------|-------|---------------|-------|----------------|-------|
| Ensemble solid of<br><b>CPHATN-1a</b> | 470                         | 1.1           | 80    | 18            | 10    |                | 10    |
|                                       | 480                         | 1.1           | 79    | 20            | 11    |                | 10    |
|                                       | 500                         | 1.2           | 43    | 22            | 45    |                | 12    |
|                                       | 520                         | 1.2           | 17    | 22            | 63    |                | 20    |
|                                       | 540                         | 0.8           | -100  | 18            | 78    | 190*           | 22    |
|                                       | 550                         | 1.0           | -100  | 18            | 72    |                | 28    |
|                                       | 560                         | 1.2           | -100  | 21            | 70    |                | 30    |
|                                       | 580                         | 1.1           | -100  | 20            | 73    |                | 27    |
|                                       | 600                         | 1.2           | -100  | 22            | 28    |                | 72    |

nm) to 75% when the excitation shifts from 371 to 470 nm, respectively. As we said above, this component reflects the emission from the initially excited state. After excitation, few of these species may exhibit an ICT process. Therefore, when we pump with a lower energy (470 nm), some structures may not undergo the ICT event, and the *emission intensity from the initially pumped state increases*. However, when we excite with more excess energy (370 nm), a larger population of these species could undergo the ICT reaction, which is reflected by a decrease in the contribution of the shortest component. This behavior indicates the presence of an energy barrier between the potential-energy surfaces of the initially excited structures and the formed ICT species.

**Femtosecond Time-Resolved Experiments.** To explore the ultrafast processes, we carried out femtosecond (fs) experiment on **CPHATN-1a** in solid state. We excited at 400 nm and gated the emission at different wavelengths. Figure 7 shows the fs emission transients decays in a short time-window, while Figure S11 displays the

complete decays. Using a multiexponential model to fit the emission decays, we obtained three time constants with values of 1.1, 20 and 190 ps, being the longest one a fixed value in the fit, and using that of the picosecond data (Table 3). The shortest component is decaying at the bluest part, and becomes a rise from 540 nm; while the other ones are decaying over the all emission spectrum. Note also that the up-conversion signals at 470-520 show an ultrafast rise, which is under the time resolution of the setup ( $\sim 100$  fs). Taking into account the spectral position of the ultrafast ( $\leq 100$  fs) and fast (1.1 ps) components, we suggest the following assignments, in agreement with that already discussed in the ps-part. The ultrafast rising component at the bluest emission region reflects the ICT reaction, while the 1.1 ps value (decay and rise) is due to intermolecular proton transfer between the acid groups of the fundamental units of the crystals. The 20 ps component most probably originates from structures having suffered a fast crossing to the dark ( $n, \pi^*$ ) states, as we previously mentioned. Moreover, it is well known that this kind of materials (HOFs, MOFs and COFs) are not



free from defects, which can change their photophysical properties.<sup>27</sup> Defects can also be very beneficial for LED and photocatalysis applications.<sup>28</sup> These defects enhance no radiative transitions. In the following part, we examine the emission lifetime and spectra at single and several crystals for getting further knowledge on the effect of defects on their photobehaviour.

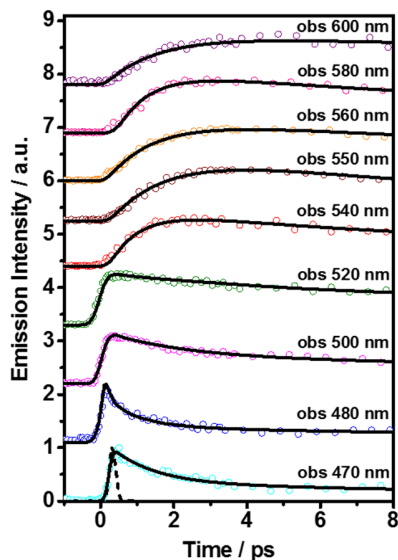


**Figure 7:** Representative femtosecond emission transients of CPHATN-1a in solid state upon excitation at 400 nm. The observation wavelengths are indicated in the inset. The solid lines are from the best fit using a multiexponential function, and the dash line denotes the instrumental response function (IRF).

**Confocal Microscopy Fluorescence and Time-Resolved Studies.** To elucidate the effect of the size, cracking and possible defects on the photodynamics, we performed confocal fluorescence microscopy studies of single crystals. Figure 8a shows the fluorescence image (FLIM) of a representative single crystal of around 35  $\mu\text{m}$  in length. Figure 8b displays the emission spectra at different selected points of the crystal. Interestingly, we observed a spectral red-shift between the points 1-3 and 4-9. It turns out that points 1-3 are on the cracks and borders of the signal crystal (Figure 8a). This behavior has been also observed on similar HOF.<sup>10b</sup> As we said above, this kind of materials are not free from defects, which can change their photophysical properties. Furthermore, we performed the same experiments on crystals of different sizes and forms (Figure 9a and 9b, Figure S12a, S12b, S13a and S13b). The emission spectra show a small red-shift, as we observed for the single crystal.

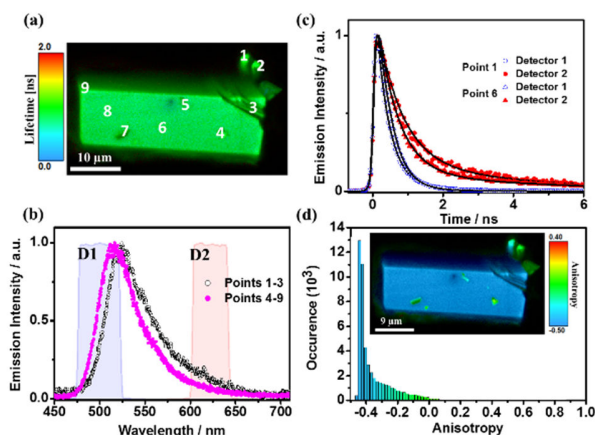


**Figure 8:** a) Fluorescence image of a single CPHATN-1a crystal. b) Emission spectra at different points of the related crystal. c) Emission decays at selected spectral range using two different filters of transmission to gate at D1 or at D2 region as shown in (b). For detector 1 (D1), we used a FF01-625-32-25 Chroma filter, and for detector 2 (D2) we used a FF01-503-40-25 Chroma filter. The solid lines are from the best-fit using a multiexponential function. d) Histogram of the emission anisotropy for the related crystal. The excitation wavelength was 390 nm.

We also collected the ps-emission decays at the same positions for the emission spectra, although we only show representative ones (Figures 8c, 9c, S12c and S13c). The decays were recorded at two different regions of the emission spectrum using two detectors: detector 1 (D1) for the blue-green emission region (475-525 nm) and detector 2 (D2) for the red one (600-650 nm). Table 4 shows a summary of the obtained results using a multiexponential fit of the decays, while table S4 gives the obtained lifetimes and pre-exponential values. Interestingly, gating at the blue-green region (D1), we obtained time values of 220-400 ps and 0.5-0.6 ns; while recording at the red part (D2) we got 500-700 ps and 2.7-3.7 ns. These values are comparable to 190 ps, 507 ps and 2.71 ns lifetimes obtained from the ps-experiments on the ensemble. Therefore, the shortest component comes from the initially excited state, while the 500-700 ps is attributed to species having suffered an ICT process. Finally, the longest lifetime (2.7-3.7 ns) is assigned to the species formed after an intermolecular proton-transfer reaction in the crystal.

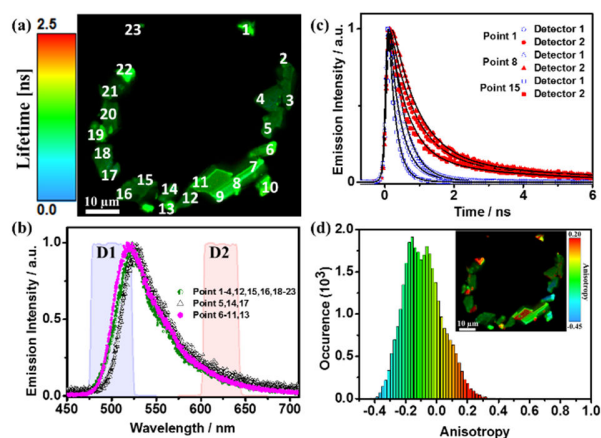


**Figure 9:** a) FLIM of CPHATN-1a crystals. b) Emission spectra at different points of the crystals. c) Emission decays at selected spectral range using two different filters (D1 and D2 in (b)). The solid lines are from the best-fit using a multiexponential function. d) Histogram of the emission anisotropy for the shown FLIM. The excitation wavelength was 390 nm.

To end, fluorescence confocal microscopy measurements on CPHATN-1a crystals show high anisotropic emission behavior (Figure 8d). The anisotropy displays a value of -0.44, which corresponds to a parallel orientation to the observation plane. Moreover, there is a low population, which exhibits an anisotropy centered at -0.2. Taking into account the anisotropy image, we observe that the large and main crystal displays the more negative value, while the smallest ones adsorbed on the surface of the main crystal, and also the defects of the main crystal display other values, which form the tail of the anisotropy. The different values reflect the different disposition of the crystals. Similar behavior has been found for CPHAT-1a and CBPHAT-1a.<sup>10</sup> Therefore, the anisotropic behavior suggests that the crystalline structure of CPHATN-1a has a preferential orientation of the molecular dipole moments perpendicular to the long axis with the  $\pi$ - $\pi$  stacking. This fact is also supported by the results from other crystals. For example, Figure 9d presents the anisotropy histogram of several crystals. The histogram is large, clearly reflecting the different orientations of the crystals. Furthermore, Figure S12d shows the result of another large crystal. The histogram presents two maxima at -0.1 and 0.67 and a shoulder at 0.46. The highest occurrence corresponds to the large crystal which is vertically oriented, contrary to one of a negative anisotropy (-0.44), horizontally orientation (Figure 8d).

**Table 4.** Summary of the values of time constants ( $\tau_i$ ) and normalized (to 100) pre-exponential factors ( $A_i$ ) obtained from the fit of the emission decays of the different points of the different point and crystals of CPHATN-1a.

| Image of Figure | Detector | $\tau_1$ (ps)<br>$\pm 50$ ps | $A_1$   | $\tau_2$ (ns)<br>$\pm 0.2$ ns | $A_2$   |
|-----------------|----------|------------------------------|---------|-------------------------------|---------|
| 8               | 1        | 220 - 300                    | 96 - 98 | 0.5 - 0.6                     | 4 - 2   |
|                 | 2        | 540 - 600                    | 84 - 90 | 2.7 - 3.0                     | 16 - 10 |
| 9               | 1        | 240 - 300                    | 96 - 98 | 0.5 - 0.6                     | 4 - 2   |
|                 | 2        | 500 - 600                    | 84 - 91 | 2.7 - 3.0                     | 16 - 9  |
| S12             | 1        | 280 - 310                    | 96 - 98 | 0.5 - 0.6                     | 6 - 2   |
|                 | 2        | 600 - 660                    | 82 - 90 | 2.9 - 3.0                     | 18 - 10 |
| S13             | 1        | 300 - 400                    | 96 - 98 | 0.6 - 0.7                     | 4 - 2   |
|                 | 2        | 600 - 700                    | 82 - 94 | 3.2 - 3.7                     | 18 - 6  |

**Acid-induced Color Changes.** It is remarkable that CPHATN-1a shows color changes by exposing it to HCl. As shown in Figure 10a, yellow crystalline bulks of CPHATN-1a immediately turned into redish-brown by adding a drop of 37%-HCl aqueous solution. Subsequence heating of the brown bulks resulted into recovery of the original yellow color due to removal of HCl. Note that the acid-responsive color change observed in solid state was not observed in solution of CPHATN-1a (Figures S14, S15). This characteristic color changes observed only for the solid state suggests that protonated HATN core might strongly interacts with the adjacent HATN cores to form strongly coupled species such as a CT complex.

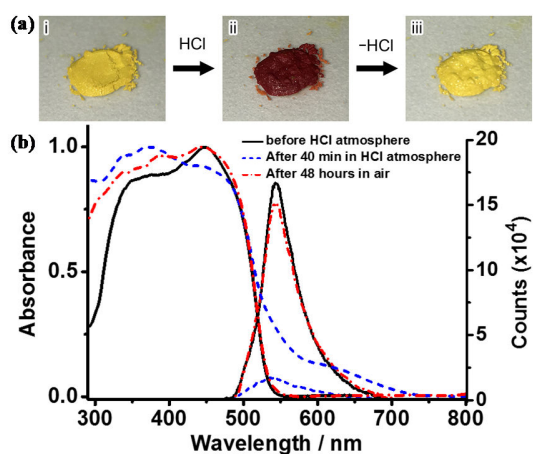


**Figure 10.** (a) HCl-responsive color changes of crystalline bulks of **CPHATN-1a** (i) before exposure, (ii) after dropped 37%-HCl on, and (iii) after heating at 423 K for 30 min. (b) Absorption and emission spectra of solid **CPHATN-1a** upon exposing it during 40 minutes in HCl atmosphere, and after leaving the exposed crystals in air during 48 h.

To obtain structural information of **CPHATN-1a** upon HCl exposing, PXRD pattern of the crystalline bulks were recorded before exposure, after adding a drop of 37%-HCl, and after heating at 423 K for 30 min (Figure S16). The PXRD patterns were once disappeared by adding a HCl drop and the original pattern is then completely recovered after heating. This tendency is the same as that for the HCl soaked samples (Figure 4). The disappearance of the patterns is presumably attributed to (1) disorder of the framework by adding HCl and/or (2) scattering or absorption of diffracted X-ray by disordered Cl<sup>-</sup> ions or water molecules filling the void. To exclude the second factor, **CPHATN-1a** was exposed to a vapor of HCl. Color was changed upon exposing to HCl vapor (Figure S17) and simultaneously new peaks at 4.86, 5.78, 9.78, 11.7° appeared in PXRD patterns in addition to the original peaks (Figure S18), indicating that protonation of the core perturbs the structure of the original framework. The new peaks disappeared when the sample was heated to remove HCl and back to the original yellow solid.

When the HOF crystals are exposed to HCl vapors, the absorption and emission spectra show insignificant changes (Figure 10b). The absorption spectrum exhibits a new band at 500-600 nm. While the emission one is strongly quenched. These observations clearly indicate the sensitivity of this HOF to acid vapors, and explained in terms of strong interactions of the protons acid with the core of the fundamental unit, as we said above. Interestingly, the original absorption and emission

spectra are ~90% recovered by clearing the HOF crystals in air and at ambient temperature and during 48 h (Figure 10b). Thus, we can use this HOF as sensor of acid atmospheres for several times. Furthermore, we recorded ps-emission decays of the HOF exposed to HCl vapor (Figure S19). We excited at 470 nm where the protonated crystals absorbs. The decays show a multiexponential behaviour with time constants of 73 ps, 360 ps and 1.81 ns (table S5). All the components are decaying over the all spectral range, while the contribution of the shortest component decreases in the red part, the others two increase. The times constants are shorter than those of original HOF (190, 507 ps and 2.51 ns), in agreement with the strong quenching observed in the emission spectrum. Because 470 nm excitation will also pump a population of not protonated HOF, the recorded decays should be a combination of protonated and not protonated crystals.

## CONCLUSION

In this work, we demonstrated for the first time that hexaazatrinaphthylene derivatives with carboxy phenyl groups (**CPHATN**) can be a suitable building block to construct acid responsive porous crystalline materials. Facile recrystallization of **CPHATN** solution gave a hydrogen-bonded organic framework (HOF) with layered structure of a hexagonal network. Precise structures of both 1,2,4-trichlorobenzene solvate [**CPHATN-1(TCB)**] and activated HOF with permanent porosity (**CPHATN-1a**) were successfully determined by single-crystalline X-ray diffraction analysis. Permanent porosity of **CPHATN-1a** was evaluated by gas sorption experiments at low temperature. Thermal stability of **CPHATN-1a** was also evaluated by VT-PXRD, disclosing its stability up to at least 633 K. fs-ps time-resolved emission experiments indicate the occurrence of an ICT ( $\leq 200$  fs) and intermolecular proton transfer (1.2 ps) reactions in the HOF. Single crystal fluorescence microscopy reveals the high orientation of the units to form the crystals; and shows the importance of defects and cracking in their photobehaviour. Remarkably, **CPHATN-1a** exhibits a reversible acid-induced color changes and ON/OFF of its emission, due to protonation/deprotonation of the pyridyl nitrogen atoms embedded in its  $\pi$ -conjugated core. Thus, we believe that the present system provides new in-sights for developing stimuli responsive HOFs.

## ASSOCIATED CONTENT

**Supporting Information.** Details of synthesis and characterization, photophysical properties, and photographs for color changes of the HOF, crystallographic information files (CIFs) of **CPHATN-1(TCB)**, **CPHATN-1a**, and **CPHATN-NP**

(CCDC1877479-1877481). This material is available free of charge via the Internet at <http://pubs.acs.org>.”

## AUTHOR INFORMATION

### Corresponding Author

\* hisaki@es.hokudai.ac.jp

\* Abderrazzak.Douhal@uclm.es

### ORCID

Ichiro Hisaki: 0000-0002-8170-5605

Eduardo Gomez: 0000-0002-0079-7852

Norimitsu Tohnai: 0000-0001-7051-7599

Abderrazzak Douhal: 0000-0003-2247-7566

### Author Contributions

† Y.S. and E.G. contributed equally.

### Notes

The authors declare no competing financial interest.

## ACKNOWLEDGMENT

This work is supported by a Grant-in-Aid for Scientific Research (C) (JP15K04591 to I.H.) and (B) (JP18H01966 to I.H.) and by the MINECO through projects MAT2014-57646-P and MAT2017-86532-R to A.D. E.G. thanks the MINECO for the PhD fellowship: FPU15/01362. PXRD measurements under gas absorption-desorption conditions was conducted at BL38B1 and BL02B2 in SPring-8 with approval of JASRI (proposal Nos. 2017B1322, 2018A1327, 2017B1325, and 2018A1238).

## REFERENCES

- (a) Slater, A. G.; Cooper, A. I., Porous materials. Functioned design of new porous materials. *Science*, **2015**, *348*, aaa8075. (b) Das, S.; Heasman, P. Ben, T.; Qiu, S., Porous organic materials: strategic design and structure-function correlation. *Chem. Rev.* **2017**, *117*, 1515.
- Côté, A. P.; Benin, A. I.; Ockwig, N. W.; O’Keeffe, M.; Matzger, A. J.; Yaghi, O. M., Porous, crystalline, covalent organic frameworks. *Science* **2005**, *310*, 1166.
- (a) Feng, X.; Ding, X.; Jiang, D., Covalent organic frameworks. *Chem. Soc. Rev.* **2012**, *41*, 6010. (b) Ding, S.-Y.; Wang, W., Covalent organic frameworks (COFs): from design to applications. *Chem. Soc. Rev.* **2013**, *42*, 548. (c) Dogru, M.; Bein, T., On the road towards electroactive covalent organic frameworks. *Chem. Commun.* **2014**, *50*, 5531. (d) Waller, P. J.; Gandara, F.; Yaghi, O. M., Chemistry of covalent organic frameworks. *Acc. Chem. Res.* **2015**, *48*, 3053. (e) Zhao, W.; Xia, L.; Liu, X., Covalent organic frameworks (COFs): perspectives of industrialization. *CrystEngComm* **2018**, *20*, 1613.
- (a) Luo, J.; Wang, J.-W.; Zhang, J.-H.; Lai, S.; Zhong, D.-C., Hydrogen-bonded organic frameworks: design, structures and potential applications. *CrystEngComm* **2018**, *20*, 5884. (b) Lu, J.; Cao, R., Porous organic molecular frameworks with extrinsic porosity: a platform for carbon storage and separation. *Angew. Chem. Int. Ed.* **2016**, *55*, 9474.
- For examples, see; (a) Yang, W.; Greenaway, A.; Lin, X.; Matsuda, R.; Blake, A. J.; Wilson, C.; Lewis, W.; Hubberstey, P.; Kitagawa, S.; Champness, N. R.; Schröder, M., A robust binary supramolecular organic framework (SOF) with high CO<sub>2</sub> adsorption and selectivity. *J. Am. Chem. Soc.* **2010**, *132*, 14457. (b) Tian, J.; Zhou, T.-Y.; Zhang, S.-C.; Aloni, S.; Altoe, M. V.; Xie, S.-H.; Wang, H.; Zhang, D.-W.; Zhao, X.; Liu, Y.; Li, Z.-T., Three-dimensional periodic supramolecular organic framework ion sponge in water and microcrystals. *Nat. Commun.* **2014**, *5*, 5574.
- (a) Yin, Q.; Zhao, P.; Sa, R.-J.; Chen, G.-C.; Lü, J.; Liu, T.-F.; Cao, R., An ultra-robust and crystalline redeemable hydrogen-bonded organic framework for synergistic chemophotodynamic therapy. *Angew. Chem. Int. Ed.* **2018**, *57*, 7691. (b) Yamagishi, H.; Sato, H.; Hori, A.; Sato, Y.; Matsuda, R.; Kato, K.; Aida, T., Self-assembly of lattices with high structural complexity from a geometrically simple molecule. *Science* **2018**, *361*, 1242.
- (a) He, Y.; Xiang, S.; Chen, B., A microporous hydrogen-bonded organic framework for highly selective C<sub>2</sub>H<sub>2</sub>/C<sub>2</sub>H<sub>4</sub> separation at ambient temperature. *J. Am. Chem. Soc.* **2011**, *133*, 14570. (b) Wang, H.; Li, B.; Wu, H.; Hu, T.-L.; Yao, Z.; Zhou, W.; Xiang, S.; Chen, B., A flexible microporous hydrogen-bonded organic framework for gas sorption and separation. *J. Am. Chem. Soc.* **2015**, *137*, 9963. (c) Hisaki, I.; Nakagawa, S.; Suzuki, Y.; Tohnai, N., CO<sub>2</sub> Sorption of layered hydrogen-bonded organic framework causes reversible structural changes involving four different crystalline states under ambient pressure. *Chem. Lett.* **2018**, *47*, 1143.
- (a) Maly, K. E.; Gagnon, E.; Maris, T.; Wuest, J. D., Engineering hydrogen-bonded molecular crystals built from derivatives of hexaphenylbenzene and related compounds. *J. Am. Chem. Soc.* **2007**, *129*, 4306. (b) Yang, J.; Dewal, M. B.; Profeta, S.; Smith, Jr., M. D.; Li, Y.; Shimizu, L. S., Origins of selectivity for the [2+2] cycloaddition of  $\alpha,\beta$ -unsaturated ketones within a porous self-assembled organic Framework. *J. Am. Chem. Soc.* **2008**, *130*, 612. (c) Comotti, A.; Bracco, S.; Distefano, G.; Sozzani, P., Methane, carbon dioxide and hydrogen storage in nanoporous dipeptide-based materials. *Chem. Commun.* **2009**, 284. (d) Mastalerz, M.; Oppel, I., Rational construction of an extrinsic porous molecular crystal with an extraordinary high specific surface area. *Angew. Chem. Int. Ed.* **2012**, *51*, 5252. (e) Luo, X.-Z.; Jia, X.-J.; Deng, J.-H.; Zhong, J.-L.; Liu, H.-J.; Wang, K.-J.; Zhong, D.-C., A microporous hydrogen-bonded organic framework: exceptional stability and highly selective adsorption of gas and liquid. *J. Am. Chem. Soc.* **2013**, *135*, 11684. (f) Lü, J.; Perez-Krap, C.; Suyetin, M.; Alsmail, N. H.; Yan, Y.; Yang, S.; Lewis, W.; Bichoutskaia, E.; Tang, C. C.; Blake, A. J.; Cao, R.; Schröder, M., A robust binary supramolecular organic framework (SOF) with high CO<sub>2</sub> adsorption and selectivity. *J. Am. Chem. Soc.* **2014**, *136*, 12828. (g) Comotti, A.; Bracco, S.; Yamamoto, A.; Beretta, M.; Hirukawa, T.; Tohnai, N.; Miyata, M.; Sozzani, P., Engineering switchable rotors in molecular crystals with open porosity. *J. Am. Chem. Soc.* **2014**, *136*, 618. (h) Chen, T.-H.; Popov, I.; Kaveevivitchai, W.; Chuang, Y.-C.; Chen, Y.-S.; Daugulis, O.; Jacobson, A. J.; Miljanić, O. Š., Thermally robust and porous noncovalent organic framework with high affinity for fluorocarbons and CFCs. *Nat. Commun.* **2014**, *5*, 5131. (i) Li, P.; He, Y.; Zhao, Y.; Weng, L.; Wang, H.; Krishna, R.; Wu, H.; Zhou, W.; O’Keeffe, M.; Han, Y.; Chen, B., A rod-packing microporous hydrogen-bonded organic framework for highly selective separation of C<sub>2</sub>H<sub>2</sub>/CO<sub>2</sub> at room temperature. *Angew. Chem. Int. Ed.* **2015**, *54*, 574. (j) Yadav, V. N.; Comotti, A.

- Sozzani, P.; Bracco, S.; Bonge-Hansen, T.; Hennum, M.; Görbitz, C. H., Microporous molecular materials from dipeptides containing non-proteinogenic sesidues. *Angew. Chem. Int. Ed.* **2015**, *54*, 15684. (k) Zentner, C. A.; Lai, H. W. H.; Greenfield, J. T.; Wiscons, R. A.; Zeller, M.; Campana, C. F.; Talu, O.; FitzGerald, S. A.; Rowsell, J. L. C., High surface area and Z' in a thermally stable 8-fold polycatenated hydrogen-bonded framework. *Chem. Commun.* **2015**, *51*, 11642. (l) Nandi, S.; Chakraborty, D.; Vaidhyanathan, R., A permanently porous single molecule H-bonded organic framework for selective CO<sub>2</sub> capture. *Chem. Commun.* **2016**, *52*, 7249. (m) Yang, W.; Wang, J.; Wang, H.; Bao, Z.; Zhao, J. C.-G.; Chen, B., Highly Interpenetrated Robust Microporous Hydrogen-Bonded Organic Framework for Gas Separation. *Cryst. Growth Des.* **2017**, *17*, 6132. (n) Hu, F.; Liu, C.; Wu, M.; Pang, J.; Jiang, F.; Yuan, D.; Hong, M., An ultrastable and easily regenerated hydrogen-bonded organic Mmolecular framework with permanent porosity. *Angew. Chem. Int. Ed.* **2017**, *56*, 2101. (o) Hashim, M. I.; Le, H. T. M.; Chen, T.-H.; Chen, Y.-S.; Daugulis, O.; Hsu, C.-W.; Jacobson, A. J.; Kaveevivitchai, W.; Liang, X.; Makarenko, T.; Miljanić, O. Š.; Popovs, I.; Tran, H. V.; Wang, X.; Wu, C.-H.; Wu, J. I., Dissecting porosity in molecular crystals: influence of geometry, hydrogen bonding, and  $[\pi\cdots\pi]$  stacking on the solid-state packing of fluorinated aromatics. *J. Am. Chem. Soc.* **2018**, *140*, 6014.
9. (a) Hisaki, I.; Nakagawa, S.; Tohnai, N.; Miyata, M., A C<sub>3</sub>-symmetric macrocycle-based, hydrogen-bonded, multiporous hexagonal network as a motif of porous molecular crystals. *Angew. Chem. Int. Ed.* **2015**, *54*, 3008. (b) Hisaki, I.; Ikenaka, N.; Tohnai, N.; Miyata, M., Polymorphs of layered assemblies of hydrogen-bonded hexagonal networks caused by conformational frustration. *Chem. Commun.* **2016**, *52*, 300. (c) Hisaki, I.; Nakagawa, S.; Ikenaka, N.; Imamura, Y.; Katouda, M.; Tashiro, M.; Tsuchida, H.; Ogoshi, T.; Sato, H.; Tohnai, N.; Miyata, M., A series of layered assemblies of hydrogen-bonded, hexagonal networks of C<sub>3</sub>-symmetric  $\pi$ -conjugated molecules: a potential motif of porous organic materials. *J. Am. Chem. Soc.* **2016**, *138*, 6617. (d) Hisaki, I.; Nakagawa, S.; Sato, H.; Tohnai, N., Alignment of paired molecules of C<sub>60</sub> within a hexagonal platform networked through hydrogen-bonds. *Chem. Commun.* **2016**, *52*, 9781. (e) Hisaki, I.; Affendy, N. Q. E.; Tohnai, N., Precise elucidations of stacking manners of hydrogen-bonded two-dimensional organic frameworks composed of X-shaped  $\pi$ -conjugated systems. *CrystEngComm* **2017**, *19*, 4892. (f) Hisaki, I.; Toda, H.; Sato, H.; Tohnai, N.; Sakurai, H., A hydrogen-bonded hexagonal bucky bowl framework. *Angew. Chem. Int. Ed.* **2017**, *56*, 15294. (g) Hisaki, I.; Ikenaka, N.; Tsuzuki, S.; Tohnai, N., Sterically crowded hydrogen-bonded hexagonal network frameworks. *Mater. Chem. Front.* **2018**, *2*, 338.
  10. (a) Hisaki, I.; Ikenaka, N.; Gomez, E.; Cohen, B.; Tohnai, N.; Douhal, A. Hexaazatriphenylene-based hydrogen-bonded organic framework with permanent porosity and single-crystallinity. *Chem. Eur. J.* **2017**, *23*, 11611. (b) Hisaki, I.; Suzuki, Y.; Gomez, E.; Cohen, B.; Tohnai, N.; Douhal, A., Docking strategy to construct thermostable, single-crystalline, hydrogen-bonded organic framework with high surface area. *Angew. Chem. Int. Ed.* **2018**, *57*, 12650.
  11. For a review; Segura, J. L.; Juárez, R.; Ramos, M.; Seoane, C., Hexaazatriphenylene (HAT) derivatives: from synthesis to molecular design, self-organization and device applications. *Chem. Soc. Rev.* **2015**, *44*, 6850.
  12. Skujins, S.; Webb, G. A., Spectroscopic and structural studies of some oxocarbon condensation products—I: Preparation and characterization of some substituted phenazines and quinoxalines. *Tetrahedron* **1969**, *25*, 3935.
  13. (a) Crispin, X.; Cornil, J.; Friedlein, R.; Okudaira, K. K.; Lemaure, V.; Crispin, A.; Kestemont, G.; Lehmann, M.; Fahlman, M.; Lazzaroni, R.; Geerts, Y.; Wendin, G.; Ueno, N.; Brédas, J.-L.; Salaneck, R., Electronic delocalization in discotic liquid crystals: a joint experimental and theoretical study. *J. Am. Chem. Soc.* **2004**, *126*, 11889. (b) Lehmann, M.; Kestemont, G.; Aspe, R. G.; Buess-Herman, C.; Koch, M. H. J.; Debije, M. G.; Piris, J.; de Haas, M. P.; Warman, J. M.; Watson, M. D.; Lemaure, V.; Cornil, J.; Geerts, Y. H.; Gearba, R.; Ivanov, D. A., High charge-carrier mobility in p-deficient discotic mesogens: design and structure-property relationship. *Chem. Eur. J.* **2005**, *11*, 3349. (c) Barlow, S.; Zhang, Q.; kaafarani, B. R.; Risko, C.; Amy, F.; Chan, C. K.; Domercq, B.; Starikova, Z. A.; Antipin, M. Y.; Timofeeva, T. V.; Kippelen, B.; Brédas, J.-L.; Kahn, A.; Marder, S. R., Synthesis, ionisation potentials and electron affinities of hexaazatriphenylene derivatives. *Chem. Eur. J.* **2007**, *13*, 3537-3547. (d) Sim, R.; Ming, W.; Setiawan, Y.; Lee, P. S., Dependencies of donor-acceptor memory on molecular levels. *J. Phys. Chem. C* **2013**, *117*, 677. (e) Selzer, F.; Falkenberg, C.; Hamburger, M.; Baumgarten, M.; Müllen, K.; Leo, K.; Moritz, R., Improved organic p-i-n type solar cells with n-doped fluorinated hexaazatriphenylene derivatives HATNA-F<sub>6</sub> and HATNA-F<sub>12</sub> as transparent electron transport material. *J. Appl. Phys.* **2014**, *115*, 054515. (f) Zhao, D.; Zhu, Z.; Kuo, M.-Y.; Chueh, C.-C.; Jen, A. K.-Y., Hexaazatriphenylene derivatives: efficient electron-transporting materials with tunable energy levels for inverted perovskite solar cells. *Angew. Chem. Int. Ed.* **2016**, *55*, 8999.
  14. (a) Catalano, V. J.; Larson, W. E.; Olmstead, M. M.; Gray, H. B., Mononuclear and binuclear palladium(II)/rhenium(I) complexes containing a sterically hindered trinucleating Ligand: 2,3,8,9,14,15-Hexamethyl-5,6,11,12,17,18-hexaazatriphenylene (hhtn) *Inorg. Chem.* **1994**, *33*, 4502. (b) Piglosiewicz, I. M.; Beckhaus, R.; Saak, W.; Haase D., Dehydroaromatization of quinoxalines: one-step syntheses of trinuclear 1,6,7,12,13,18-hexaazatriphenylene titanium complexes. *J. Am. Chem. Soc.* **2005**, *127*, 14190. (c) Roy, S.; Sarkar, B.; Duboc, C.; Fiedler, J.; Sarper, O.; Lissner, F.; Mobin, S. M.; Lahiri, G. K.; Kaim, W., Heterohexanuclear (Cu<sub>3</sub>Fe<sub>3</sub>) complexes of substituted hexaazatriphenylene (HATN) ligands: twofold BF<sub>4</sub><sup>-</sup> association in the solid and stepwise oxidation (3e) or reduction (2e) to spectroelectrochemically characterized species. *Chem. Eur. J.* **2009**, *15*, 6932. (d) Roy, S.; Kubiak, C. P., Tricarbonylrhenium(I) complexes of highly symmetric hexaazatriphenylene ligands (HATN): structural, electrochemical and spectroscopic properties. *Dalton Trans.* **2010**, *39*, 10937. (e) Lind, S. J.; Walsh, T. J.; Blackman, A. G.; Polson, M. I. J.; Irwin, G. I. S.; Gordon, K. C., Trinuclear copper(I) complex containing 3,4,9,10,15,16-hexamethyl-1,6,7,12,13,18-hexaazatriphenylene: a structural, spectroscopic, and computational study. *J. Phys. Chem. A* **2009**, *113*, 3566. (f) Fraser, M. G.; Clark, C. A.; Horvath, R.; Lind, S. J.; Blackman, A. G.; Sun, X.-Z.; George, M. W.; Gordon, K. C., Complete

- family of mono-, bi-, and trinuclear  $\text{Re(I)(CO)}_3\text{Cl}$  complexes of the bridging polypyridyl ligand 2,3,8,9,14,15-hexamethyl-5,6,11,12,17,18-hexaazatrinaphthalene: syn/anti isomer separation, characterization, and photophysics. *Inorg. Chem.* **2011**, *50*, 6093.
15. (a) Nie, B.; Zhan, T.-G.; Zhou, T.-Y.; Xian, Z.-Y.; Jiang, G.-F.; Zhao, X., Self-assembly of chiral propeller-like supermolecules with unusual "sergeants-and-soldiers" and "majority-rules" effects. *Chem. Asian J.* **2014**, *9*, 754. (b) Li, J.; Chen, S.; Zhang, P.; Wang, Z.; Long, G.; Ganguly, R.; Li, Y.; Zhang, Q., A colorimetric and fluorimetric chemodosimeter for copper ion based on the conversion of dihydropyrazine to pyrazine. *Chem. Asian J.* **2016**, *11*, 136.
  16. Ibáñez, S.; Poyatos, M.; Peris, E., A  $D_{3h}$ -symmetry hexaazatriphenylene-tris-N-heterocyclic carbene ligand and its coordination to iridium and gold: preliminary catalytic studies. *Chem. Commun.* **2017**, *53*, 3733.
  17. (a) Grindell, R.; Vieru, V.; Pugh, T.; Chibotaru, L. F.; Layfield, R. A., Magnetic frustration in a hexaazatrinaphthylene-bridged trimetallic dysprosium single-molecule magnet. *Dalton Trans.* **2016**, *45*, 16556. (b) Gould, C. A.; Darago, L. E.; Gonzalez, M. I.; Demir, S.; Long, J. R., A Trinuclear radical-bridged lanthanide single-molecule magnet. *Angew. Chem. Int. Ed.* **2017**, *56*, 10103. (c) Lemes, M. A.; Magnan, F.; Gabidullin, B.; Brusso, J., Impact of nuclearity and topology on the single molecule magnet behaviour of hexaazatrinaphthylene-based cobalt complexes. *Dalton Trans.* **2018**, *47*, 4678.
  18. (a) Matsunaga, T.; Kubota, T.; Sugimoto, T.; Satoh, M., High-performance lithium secondary batteries using cathode active materials of triquinoxalinylenes exhibiting six electron migration. *Chem. Lett.* **2011**, *40*, 750. (b) Wang, J.; Tee, K.; Lee, Y.; Riduan, S. N.; Zhang, Y., Hexaazatriphenylene derivatives/GO composites as organic cathodes for lithium ion batteries. *J. Mater. Chem. A* **2018**, *6*, 2752.
  19. Bu, X.-H.; Biradha, K.; Yamaguchi, T.; Nishimura, M.; Ito, T.; Tanaka, K.; Shionoya, M., A novel polymeric  $\text{Ag}^{\text{I}}$  complex consisting of two three-dimensional networks which are enantiometric and interpenetrating. *Chem. Commun.* **2000**, 1953.
  20. Wöhrle, T.; Wurzbach, I.; Kirres, J.; Kostidou, A.; Kapernaum, N.; Litterscheidt, J.; Haenle, J. C.; Staffeld, P.; Baro, A.; Giesselmann, F.; Laschat, S., Discotic liquid crystals. *Chem. Rev.* **2016**, *116*, 1139.
  21. McKeown, N. B.; Cahnem, B.; Msayib, K. J.; Budd, P. M.; Tattershall, C. E.; Mahmood, K.; Tan, S.; Book, D.; Langmi, H. W.; Walton, A., Towards polymer-based hydrogen storage materials: engineering ultramicroporous cavities within polymers of intrinsic microporosity. *Angew. Chem. Int. Ed.* **2006**, *45*, 1804.
  22. Xu, F.; Chen, X.; Tang, Z.; Wu, D.; Fu, R.; Jiang, D., Redox-active conjugated microporous polymers: a new organic platform for highly efficient energy storage. *Chem. Commun.* **2014**, *50*, 4788.
  23. Xiao, R.; Tobin, J. M.; Zha, M.; Hou, Y.-L.; He, J.; Vilela, F.; Xu, Z., A nanoporous graphene analog for superfast heavy metal removal and continuous-flow visible-light photoredox catalysis. *J. Mater. Chem. A* **2017**, *5*, 20180.
  24. Yuan, F.; Li, J.; Namuangruk, S.; Kungwan, N.; Guo, J.; Wang, C., Microporous, self-segregated, graphenel polymer nanosheets prepared by dehydrogenative condensation of aza-PAHs building blocks in the solid state. *Chem. Mater.* **2017**, *29*, 3971.
  25. (a) Nishide, H.; Takahashi, M.; Takashima, J.; Pu, Y.-J.; Tsuchida, E., Acyclic and cyclic di- and tri(4-oxyphenyl-1,2-phenyleneethynylene)s: their synthesis and ferromagnetic spin interaction. *J. Org. Chem.* **1999**, *64*, 7375. (b) Tehfe, M.-A.; Dumur, F.; Xiao, P.; Zhang, J.; Graff, B.; Morlet-Savary, F.; Gigmes, D.; Fouassier, J.-P.; Lalevée, J., Photoinitiators based on a phenazine scaffold: high performance systems upon near-UV or visible LED (385, 395 and 405 nm) irradiations. *Polymer* **2014**, *55*, 2285. (c) Gomez, E.; Gutierrez, M.; Moreno, M.; Hisaki, I.; Nakagawa, S.; Douhal, A. *Phys. Chem. Chem. Phys.* **2018**, *20*, 7415. (d) Gomez, E.; Gutiérrez, M.; Cohen, B.; Hisaki, I.; Douhal, A., Spectroscopy and dynamics of dehydrobenzo[12]annulene derivatives possessing peripheral carboxyphenyl groups: theory and experiment. *J. Mater. Chem. C* **2018**, *6*, 6929-6939. (e) Wang, J.; Lee, Y.; Tee, K.; Riduan, S. N.; Zhang, Y., A nanoporous sulfur-bridged hexaazatrinaphthylene framework as an organic cathode for lithium ion batteries with well-balanced electrochemical performance. *Chem. Commun.* **2018**, *54*, 7681.
  26. Organero, J. A.; Tormo, L.; Douhal, A., Caging ultrafast proton transfer and twisting motion of 1-hydroxy-2-acetonaphthone. *Chem. Phys. Lett.* **2002**, *363*, 409.
  27. (a) Reshchikov, M. A.; Morkoç, H., Luminescence properties of defects in GaN. *J. Appl. Phys.* **2005**, *97*, 061301. (b) Fang, Z.; Bueken, B.; De Vos, D. E.; Fischer, R. A., Defect-engineered metal-organic frameworks. *Angew. Chem. Int. Ed.* **2015**, *54*, 7234. (c) Gutiérrez, M.; Martin, C.; Kennes, K.; Hofkens, J.; Van der Auweraer, M.; Sánchez, F.; Douhal, A., OLEDs Based on metal-organic framework: new OLEDs based on zirconium metal-organic framework. *Adv. Opt. Mater.* **2018**, *6*, 1701060.
  28. Dhakshinamoorthy, A.; Li, Z.; Garcia, H., Catalysis and photocatalysis by metal organic frameworks. *Chem. Soc. Rev.* **2018**, *47*, 8134.

SYNOPSIS TOC (Word Style "SN\_Synopsis\_TOC").

